Wide-Scan and Energy-Saving Phased Arrays by Exploiting Penrose Tiling Subarrays

Francesco Alessio Dicandia, and Simone Genovesi, *Senior Member, IEEE*

Abstract— **A partitioning scheme based on Penrose-inspired subarrays is proposed for wide-scan planar phased arrays. The regular triangular lattice adopted for the arrangement of the antenna elements is organized into irregularly-shaped tiles that exploit the properties offered by the Penrose tessellation. The novel array architecture ensures a remarkable reduction of the Transmit/Receive modules without harming the scan angle range and peak side lobe level thanks to the optimization based on the Pareto front that is able to tackle conflicting objectives. The performance of the proposed approach are assessed in different scenarios and prove the robustness and flexibility of the new tiling architecture. Moreover, a thorough analysis is carried out to highlight the unique feature of the partition scheme of offering a noteworthy reduction of the energy consumption.**

Index Terms—**Penrose tiles, triangular lattice, phased array antenna, multiobjective optimization, wide angle scan.**

I. INTRODUCTION

Active electronically beam-scanning antennas represent a pivotal technology for enabling efficient communications in most of the modern wireless systems and will play a more and more crucial role in coping with the ever-increasing system requirements. Beam control, low radiation pattern side lobes, multibeam [1] and Multiple-Input-Multiple-Output (MIMO) paradigm [2], [3] are only a few of the degrees of freedom that phased arrays can offer to a wireless communication system in order to guarantee the necessary quality of service. In a Fully Populated Array (FPA) each radiating element is equipped with a Transmit/Receive Module (TRM) able to control both amplitude and phase of the signal and it represents the most versatile solution for a wireless system due to the full control of the radiation pattern. However, the unrivalled performance offered by a FPA are questioned by the related cost and power consumption that are key factors in driving the evolution of the phased arrays [4] for future wireless communications as well as in the upcoming 5th one (5G). This aspect turns out to be even more important at millimeter waves frequencies where the significant losses of phase shifters and a lower Power Amplifiers (PAs) efficiency [5] also lead to a more complicated thermal management [6]. Therefore, FPAs may represent an unaffordable architecture for the newly addressed scenarios [7].

From the phased array perspective, the most straightforward strategy for both cost and power consumption reduction is represented by the reduction of the TRMs number, since they contribute for almost half of the cost of a phased array [7]. In the last years, several unconventional array architectures capable of providing a more balanced cost and performance tradeoff, and hence allowing a major dissemination of phased arrays also in civilian applications, have been proposed [8]. Sparse arrays [9]–[11] or thinned arrays [12]–[14] are some examples of unconventional array designing with the purpose of reducing TRM units. These arrays, based on an aperiodic arrangement of the radiating elements, can offer remarkable performance such as the Peak Side Lobe Level (PSLL) lowering useful to decrease interference in massive MIMO systems [15], [16]. In thinned arrays, the layout aperiodicity is generally determined by turning off some elements arranged on a regular lattice whereas antenna elements positions are optimized without the boundaries of a periodic grid in sparse arrays [17]. It is worth observing that these irregular arrays generally require complex ad-hoc feeding network designs, complicate the array calibration [18], [19] and may lead to an inefficient use of the space with a consequent aperture efficiency reduction [20].

An alternative technique, in the framework of the unconventional array architectures, is to divide the array radiating elements lying on a regular and periodic lattice in different clusters or subarrays fed by a single TRM. Therefore, each element in a subarray presents the same amplitude and phase. The simplest way of partitioning the phased array elements is to consider identical and contiguous subarrays. However, although the regular subarray technology significantly simplifies the array manufacturing, reduces the cost and could decrease the power consumption with respect to an FPA, they may exhibit limitations in angular scan range due to the onset of grating lobes inside the visible region [17] caused by the subarray periodicity. To cope with this drawback, overlapped or randomly overlapped subarrays have been proposed over the past years [21], [22]. The main downside of the overlapped subarrays is represented by the feeding network complexity that make them challenging to use in practice especially at millimeter wave frequencies [23]. Irregular but contiguous (not overlapped) subarray partitions have been proposed [24]–[27] with the aim of maintaining acceptable the

Francesco Alessio Dicandia was with Dipartimento di Ingegneria dell'Informazione, University of Pisa. (e-mail: alessio.dicandia@for.unipi.it).

Simone Genovesi is with Dipartimento di Ingegneria dell'Informazione, University of Pisa, Pisa 56122, Italy (www.dii.unipi.it). (e-mail: simone.genovesi@unipi.it).

feeding network complexity, but at the same time preserving the wide-angle beam scanning capability. In fact, these features are of the utmost importance in many applications such as 5G terrestrial or aerial base stations [28], [29], backhaul network [30], automotive radars or Device to Device (D2D) communications. Indeed, the aperiodicity at the subarray level can break the periodicity, which is typical of uniformly grouped subarrays, and therefore avoids the appearance of grating lobes and keeps at a reasonable level the radiation pattern lateral lobes. For example, in [24], [25] polyomino-shaped subarrays with an optimization of the orientation and position of the different tiles have been exploited to realized irregular clustered phased arrays. A randomly grouped subarrays capable of lowering the PSLL over a limited scan angle are also presented in [23], [31].

The purpose of this work is to propose a novel irregular and contiguous subarrays clustering technique for the design of phased arrays with large angular scanning and less energy-hungry. The innovative approach of this design is to fully exploit the potential of the Penrose tessellation for the partitioning of a periodic phased array into irregular subarrays and identifying the ones with the best performance in a multi–objective electromagnetic problem. To this end, Pareto optimal solutions to highlight the tradeoffs between two conflicting objectives will be carried out [32]. This paper is organized as follows. Section II illustrates the Penrose subarrays design approach adopted to tackle a multi–objective problem under imposed constraints. Section III describes the application of this strategy on a 16×16 phased array for achieving a complete circular scan in the *uv* plane with a θ_0 steering angle up to 60°. The minimization of the Peak Side Lobe Level (PSLL) within a rectangular scanning area with 30° in elevation ($\pm15°$) and 120° ($\pm60°$) in azimuth is illustrated in Section IV to underline both the effectiveness and the versatility of the Penrose tiling. In the following Section V, an extensive analysis regarding the power consumption and the requirements for energy-saving clustered phased array are addressed. Finally, the conclusions are reported in Section VI.

II. PENROSE SUBARRAYS DESIGN METHOD

A planar array composed by $N\times M$ elements lying on *xy* plane exhibits a radiation pattern (RP) given by:

$$RP(u,v) = \sum_{n=1}^{N}\sum_{m=1}^{M} I_{nm} e^{j\alpha_{nm}} E_{nm}(u,v) e^{j\beta(x_{nm}u + y_{nm}v)} \quad (1)$$

where $u = \sin(\theta)\cos(\phi)$, $v = \sin(\theta)\sin(\phi)$, $\beta = 2\pi/\lambda_0$ is the wave number, $E_{nm}(u,v)$ the nm^{th} element radiation pattern, I_{nm} and α_{nm} represent the amplitude and phase of the nm^{th} element, respectively, whereas x_{nm} and y_{nm} are the antenna element geometrical coordinates that depend on the employed array lattice. The radiation element phase (α_{nm}) necessary to steer the main beam in the desired direction (θ_0, ϕ_0) is equal to:

$$\alpha_{nm} = \beta\left[x_{nm}\sin(\theta_0)\cos(\phi_0) + y_{nm}\sin(\theta_0)\sin(\phi_0) \right] \quad (2)$$

In general, the irregular partition of a phased array is an open-ended problem since there are several combinations of possible

tiles capable of splitting the array into subarrays with different sizes and shapes. Therefore, Penrose tessellation has been exploited to provide irregular partitions of a phased array by studying unexplored solutions that benefit from the interesting features of aperiodic tiling as well as a deterministic procedure to cover a plane [33].

Specifically, the version known as "thick and thin" composed by a pair of isosceles triangles with internal angles 36°, 36°, 108° and 72°, 72, 36° able to cover a plane without overlaps or gaps has been exploited for the phased array partitioning optimization. Both the thick and thin isosceles triangles have two sides of length *L* whereas they differ in the third one: τL for the thick triangle whereas L/τ for the other one as shown in Fig. 1. τ represents the ratio of the area of both triangles, and it is equal to the golden ratio $\left[1 + \sqrt{5}\right]/2$.
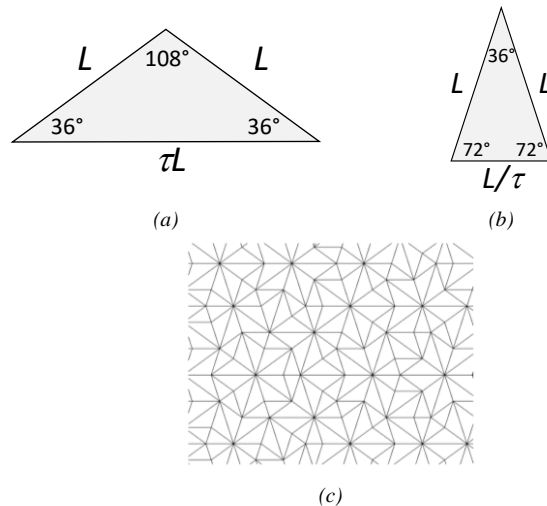

Fig. 1. Penrose's tiles: *(a)* thick isosceles triangle, *(b)* thin one and *(c)* a Penrose tessellation example.

It is worth mentioning that the Penrose tessellation has already been used in array designing but for the realization of sparse phased arrays comprising unequally spaced antenna elements [33]–[35].

In the proposed approach, possible partitions of a given array were generated through the following algorithm in order to fulfil some desired constraints:

1) Overlap the regular and periodic phased array lattice with a Penrose tiling based on the two different tiles with a defined side length *L*;
2) Generate a list with the antenna elements that can be used for the phased array partition. At the beginning the list contain all the antenna elements of the array;
3) Assign a variable $x_n = \{0,1\}$ $n = 1,\dots,K$ to all the vertex of the tessellation (*K* is the total number of vertexes of the tessellation);
4) Call a recursive partition function for all the selected vertex $x_n = 1$ by starting from the first one in the list:
    a. identify all the isosceles triangles of the tessellation that have in common the picked vertex,

b. all the antenna elements of the periodic array inside the selected isosceles triangles form a subarray,

c. remove the selected antenna elements of the periodic array from the list of the available antenna elements for the phased array partition.

5) If the list of the available antenna elements for the phased array partition is not empty, assign a single element subarray for all the elements.

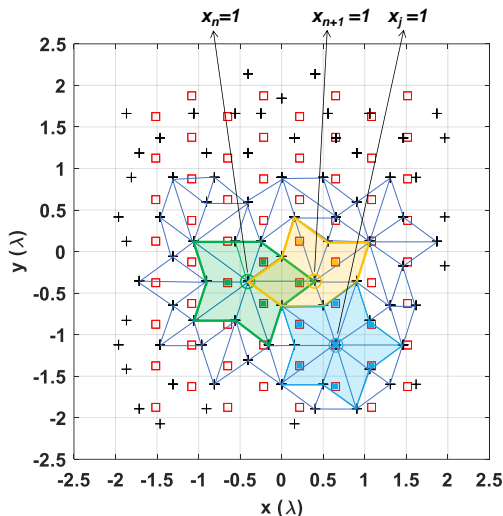To better understand the proposed algorithm, an example of a partition is shown in Fig. 2.

Fig. 2. Array composed by 8×8 elements arranged in a triangular lattice with the overlapped Penrose tessellation (blue lines). Red squares refer to the periodic element lattice whereas the black crosses ones to the Penrose's triangle vertexes.

In particular, the red squares refer to the regular and periodic array composed by 64 elements (8×8) arranged with a triangular grid whereas the black cross ones to the vertexes of a Penrose's tiles. Both the interelement spacing among antenna element and the Penrose's isosceles triangles sides length L are equal to 0.5 λ_0. For better clarify the process, the first three iterations for the creation of the subarrays are highlighted. The first vertex on the list ($x_n = 1$) is the common vertex among ten triangles of the tessellation. This area (highlighted in green) contains four array elements and are assigned to one subarray. These elements are removed from the set of available elements for other subarrays. The next selected vertex ($x_{n+1} = 1$) is the common vertex among eight triangles. This area (highlighted in yellow) hosts three array elements however only two of them are available to be part of the subarray since one element was previously assigned to another subarray and removed from the list. The succeeding selected vertex ($x_j = 1$) individuates ten triangles and seven array elements that can be grouped together since none of them was part of another subarray. In the following sections it will be shown as the Penrose's triangle sides length L as well as the number of subarrays affect the radiation performance.

If the array is divided into subarrays (Fig. 3a), the phase

related to the rth subarray (α_r), and hence to all the radiating elements belonging to the selected subarray, depend on its centroid:

$$\alpha_r = \beta \left[x_r \sin(\theta_0)\cos(\phi_0) + y_r \sin(\theta_0)\sin(\phi_0) \right] \quad (3)$$

A generic aperiodic Penrose tessellation is shown in Fig. 3b and an example of an irregular partition obtained by following this scheme is illustrated in Fig. 3c. It is apparent that the feed points number is drastically reduced by grouping the elements into irregular subarrays. More in detail, in Fig. 3c there are subarrays of different sizes that comprise up to eight elements. Subarrays with same number of elements are highlighted with the same color.
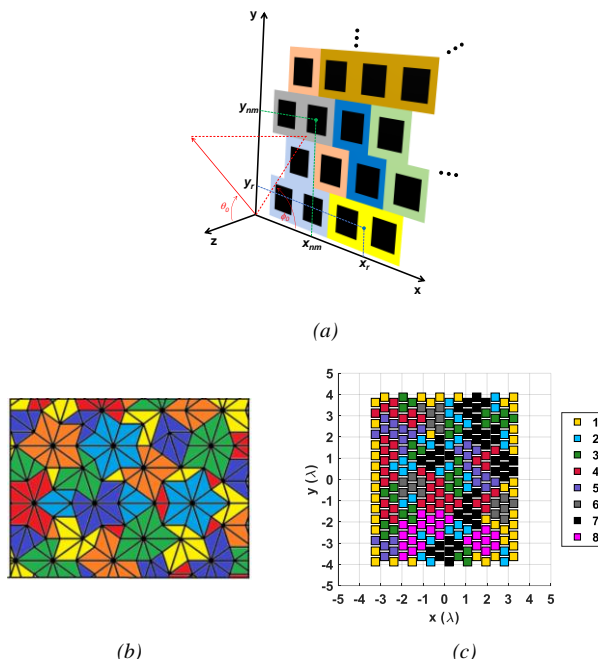

(a)

(b)   (c)

Fig. 3. (a) Planar array reference system, (b) Penrose tiling and (c) an example of a subarray partition through the Penrose tessellation approach.

III. CIRCULAR SCANNING AREA

Microwave backhauling [36], High Altitude Platform Systems (HAPSs) [29], Airborne Communication Network (ACN) employing both terrestrials and Low Orbit Earth (LEO) [37], [38] satellites are just some applications where it is important to provide a wide beam scanning in order to provide a viable communication and fulfil the systems needs such as reliability and spectral efficiency. In general, the phased array has to be characterized by radiation elements not much directive [39] to allow large scanning coverage. Indeed, the behaviour of the element's radiation pattern considerably affects the scan loss, namely the degradation of the array gain as a function of the steering angle. Phased arrays with pattern reconfigurable elements [40] have been proposed to compensate the large scan loss and broaden the scanning range [41]. However, the adoption of antenna elements with a wide beam represents certainly one of the most efficient way to alleviate the scan loss degradation [42], especially if hardware complexity and power consumption are the main concern.

The described Penrose-tessellation approach has been

adopted for the design of a 16×16 phased array able to provide a circular scanning angle in the *uv* plane with a steering angle θ_0 up to 60°. A regular and periodic triangular lattice array with an interelement spacing of 0.5 λ_0 has been taken into account for this test case. Moreover, an identical element radiation pattern equal to $E(\theta,\phi) = \sqrt{\cos(\theta)}$ has been selected to achieve a beam scanning up to 60° off broadside direction ($\theta_0 = 0°$) since it provides an Half Power Beam Width (HPBW) of 120°. It is worth noting that, the approximation of considering the same radiation pattern $E(\theta,\phi)$ for all the array elements, exploited during the array partitioning synthesis, turns out to be appropriate especially for elements arranged on a regular and periodic lattice (as in the investigated case) where most of the array antenna elements are characterized by identical mutual coupling. On the contrary, the evaluation of the different level of mutual coupling between elements is more important in sparse or thinned arrays due to the different reciprocal distances among array antenna elements [43]–[45].

The optimization of the phased array partition by resorting to the Penrose tiling subarrays has been carried out by exploiting the Pareto front algorithm implemented in MATLAB [46]. Specifically, the minimum array gain evaluated on the circle of radius sin(60°) in the *uv* plane and the thinning factor (μ), which is the TRM reduction with respect to the FPA, were used as conflicting objectives.
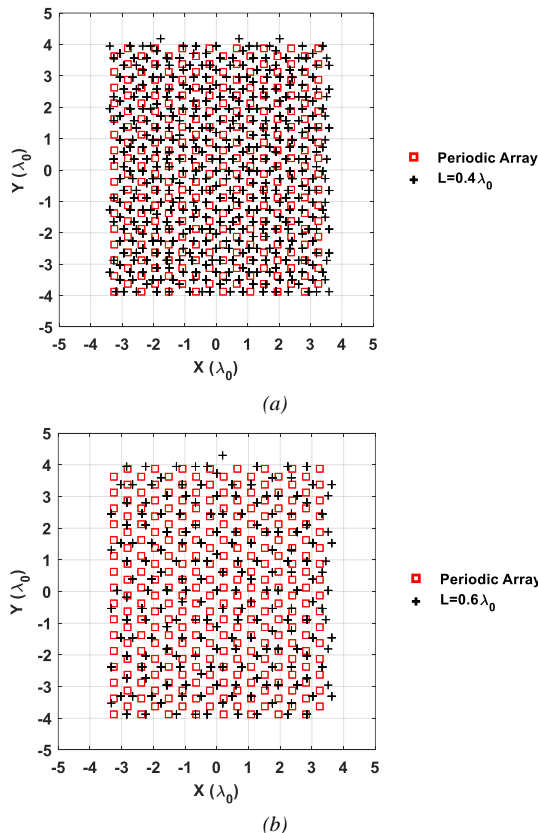

(a)

(b)

Fig. 4. Triangular lattice array composed by 16×16 elements along with the Penrose isosceles triangle vertexes in case of *(a)* $L = 0.4\,\lambda_0$ and *(b)* $L = 0.6\,\lambda_0$.

Precisely, the thinning factor (μ) is defined as:

$$\mu = 1 - \frac{N_{SA}}{N_{FPA}} \qquad (4)$$

where N_{SA} represents the number of adopted subarrays to partition the phased array whereas N_{FPA} represents the overall number of elements.

Different Penrose triangular sides length L have been used for the Penrose tiling subarrays partition. In fact, as it can be drawn from Fig. 4, given a periodic array, the L value determines the quantity of the triangle vertexes within the phased array area hence it affects the optimization process.

To implement the partition of the array, two different amplitude distributions on the phased array has been considered: uniform amplitude excitation at the subarrays level and uniform amplitude excitation at the antenna elements level. The normalized amplitude for both the schemes at the $(n,m)^{th}$ element of the array is equal to:

$$\begin{cases} a(n,m)_r = 1/\sqrt{p} & \textit{Subarrays level} \\ a(n,m) = 1 & \textit{Elements level} \end{cases} \qquad (5)$$

where p represents the total number of the antenna elements that belongs to the rth tile for the uniform amplitude excitation at the subarray level excitation scheme whereas, in case of the uniform amplitude excitation at the antenna elements, the normalized amplitude turns out to be equal to 1 for each radiating element.
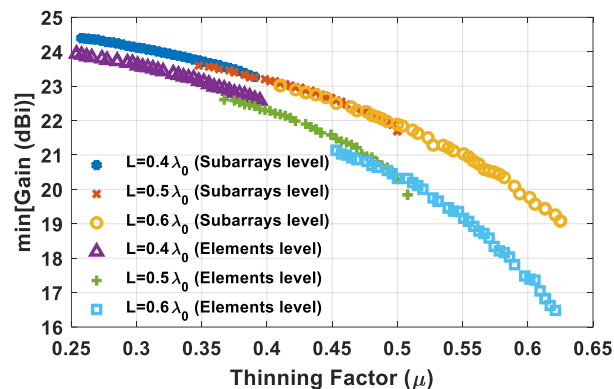

Fig. 5. Pareto front between array gain and thinning factor (μ) for different Penrose isosceles triangle sides length L in case of a uniform amplitude distributions at the subarrays level and elements level.

Fig. 5 shows the Pareto front that highlights the tradeoffs between the two conflicting objectives (*i.e.* minimum array gain and thinning factor) evaluated for different values of the triangle sides length L. In general, the greater is the thinning factor (μ) the lower is the minimum gain assessed at the maximum steering angle ($\theta_0 = 60°$) on the circle of radius equal to sin(60°). An interesting consideration can be drawn by comparing the two Pareto fronts of Fig. 5. The uniform amplitude excitation at the subarrays level (*i.e.* when all TRMs present the same output power) outperforms the uniform amplitude excitation at the antenna elements level. In fact, the unequal amplitude excitation of the radiating elements caused by the array partition introduces a further degree of freedom in the design that allows lower scan loss than the uniform

excitation scheme at element level. Moreover, the uniform element excitation requires also an unbalanced output power of the TRMs in order to provide the same amplitude $a(n,m) = 1$ to all the array antennas. For low thinning factor ($\mu < 0.35$) the Pareto fronts differ in gain about 0.65 dB but increasing the thinning factor (*i.e.* reducing the number N_{SA} of irregular but contiguous subarrays) causes a higher and higher gain difference. The superior performance of the subarray level excitation scheme turns out to be in favour also from a system perspective since, in general, Commercial Off The Shelf (COTS) TRM cannot guarantee orthogonal gain and phase control [47].
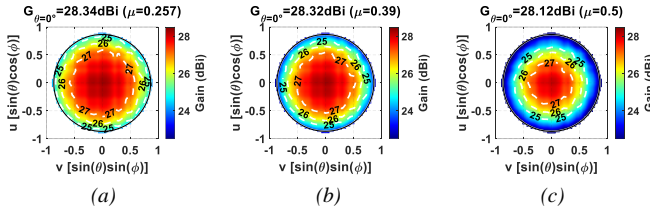

Fig. 6. Peak array gain as a function of the steering angle by exploiting the Penrose clustered arrays in case of 16×16 elements for different thinning factors (μ): *(a)* $\mu = 0.257$ (190 feed points), *(b)* $\mu = 0.39$ (156 feed points) and *(c)* $\mu = 0.5$ (128 feed points).

Therefore, any variation of the TRM amplitude (phase) provides an unwanted fluctuation of the phase (amplitude) that inevitably degrades the radiation performance such as the in-band and the out-band distortions [48].

The radiation performance of three partitions arrangement are examined in the following. Specifically, array partition layouts with a thinning factor equal to $\mu = 0.257$ (190 feed points), $\mu = 0.39$ (156 feed points) and $\mu = 0.5$ (128 feed points) have been considered.

The peak gain as a function of the main beam direction within the circular scanning range is illustrated in Fig. 6 for different thinning factors (μ).

The arrays gain presents higher values along broadside direction ($\theta_0 = 0°$) then it decreases during the main beam steering due to the beam widening as well as to the lower element's gain [17]. Even though the three phased array partitions have similar gain value around broadside direction ($G_{\theta = 0°} \in [28.12\text{-}28.34 \text{ dBi}]$), they provide considerably gain value differences with the increasing of the main beam steering ($\theta_0 > 30°$).
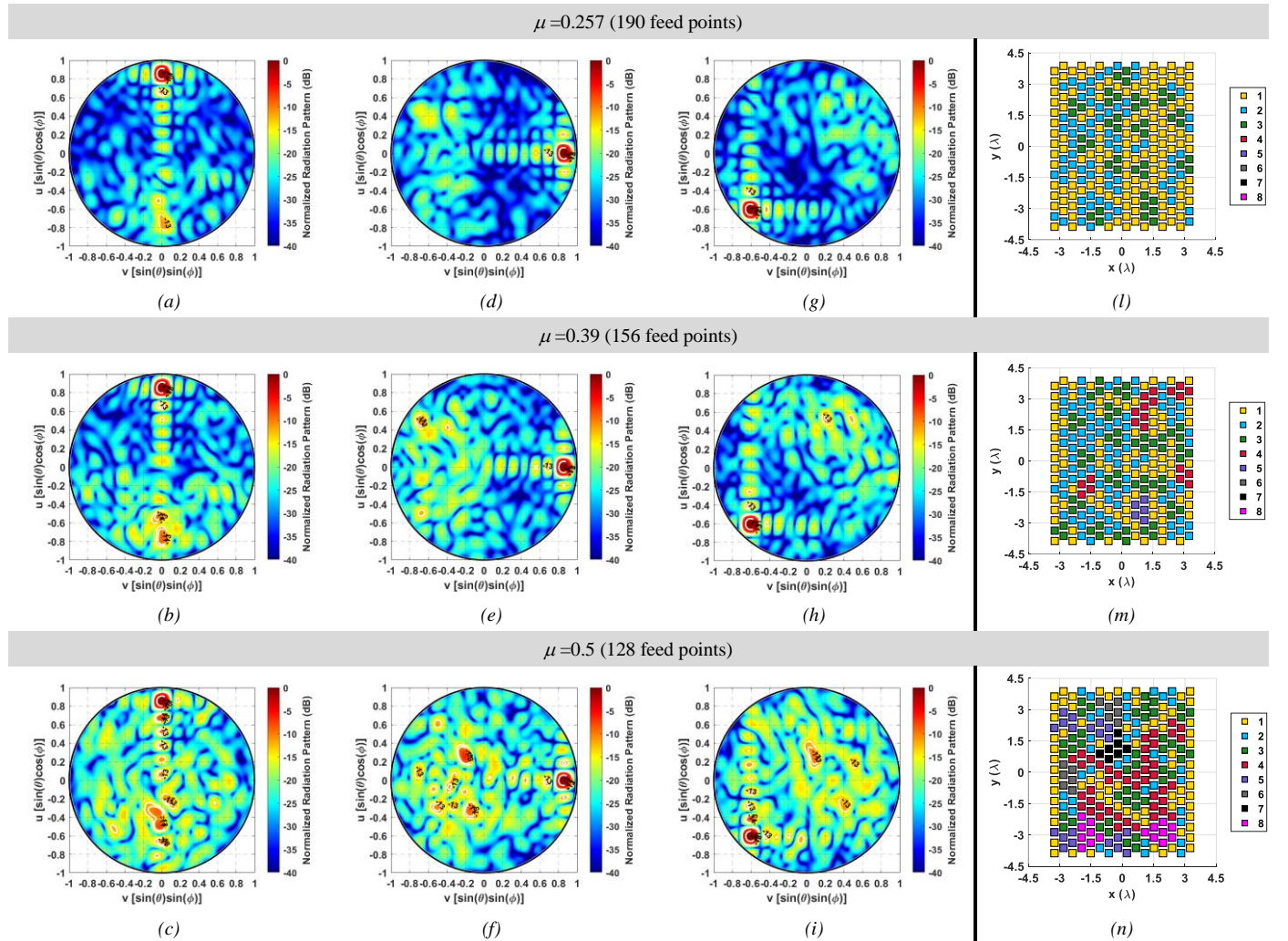

Fig. 7. Normalized radiation pattern evaluated at $\theta_0 = 60°$ and three different ϕ_0 angles by exploiting the Penrose tiling subarrays in case of 16×16 elements for various thinning factor (μ): *(a)-(c)* $\theta_0 = 60°, \phi_0 = 0°$, *(d)-(f)* $\theta_0 = 60°, \phi_0 = 90°$ *(g)-(i)* $\theta_0 = 60°, \phi_0 = 225°$ and *(l)-(n)* array partition layout.

This article has been accepted for publication in IEEE Transactions on Antennas and Propagation. This is the author's version which has not been fully edited and content may change prior to final publication. Citation information: DOI 10.1109/TAP.2022.3178917

> REPLACE THIS LINE WITH YOUR PAPER IDENTIFICATION NUMBER (DOUBLE-CLICK HERE TO EDIT) <   6
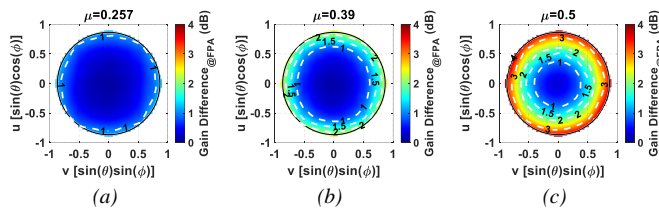
Fig. 8. Gain difference between FPA and Penrose clustered arrays as a function of the steering angle in case of 16×16 elements for different thinning factors (μ): (a) $\mu = 0.257$ (190 feed points), (b) $\mu = 0.39$ (156 feed points) and (c) $\mu = 0.5$ (128 feed points).

Colour maps of Fig. 8 better emphasize the performance worsening with respect to the FPA due to the increasing of the thinning factor as a function of the main beam steering. More in detail, a regular and contiguous Penrose tiling subarrays with $\mu = 0.257$ (190 feed point) shown in Fig. 8a provides a maximum scan loss with respect to FPA lower than 1.3 dBi inside the circular scanning area. However, a considerable worsening of the gain difference with respect to FPA occurs by increasing the thinning factor. As a matter of fact, Fig. 8c reveals that the gain difference reaches a value of 4.2 dB for $\theta_0 = 60°$, although it is worthwhile to consider that only half of the TRMs are employed.

The radiation patterns of the three partitions arrangement are reported in Fig. 7 when the main beam is steered at the edges of the field of view to show that, despite the worst-case conditions, the lateral lobes turn out to be noticeably below the main beam. As it can be inferred from the colour maps, the reduction of the TRM, in addition to the worsening of the scan loss (Fig. 8), determines a notable rise of the average side lobe levels due to a greater radiation spreading. This effect has to be carefully considered during the array design since it turns out to be harmful in different applications, such as in a multiusers scenario [29]. In fact, the increase of the average radiation over the visible region determines a worsening of the average interference and so could not allow the achievement of some predefined quality of service requirements. The array partition layouts for the three selected thinning factors are depicted in Fig. 7l-n. A thinning factor (μ) of 0.257 (190 feed points) enables to generate subarrays up to three antenna elements whereas groups up to eight radiation elements are present in case of $\mu = 0.5$ (Fig. 7n).

Table I summarizes the radiation performance in terms of peak gain ($Gain_{peak}$) and Peak Side Lobe Level (PSLL) for different scan angles and phased array partitions. From Table I it can be noticed that, as expected, FPA ($\mu = 0$) provides the best radiation performance whereas the clustered arrays present a somewhat linear degradation of the performance for both the peak gain and PSLL with respect to the thinning factor. The slight peak gain reduction at broadside direction in case of a clustered arrays ($\mu > 0$) with respect to the FPA ($\mu = 0$) is due to the uniform amplitude excitation at the subarrays level adopted scheme. In fact, as previously stated, this amplitude distribution provides an unequal amplitude level at the elements, and this determine a mild gain reduction at broadside.

TABLE I
PEAK GAIN AND PSLL FOR DIFFERENT MAIN BEAM DIRECTIONS AND PHASED ARRAY PARTITIONS OF A PLANAR ARRAY WITH 16×16 ELEMENTS.

θ_0, ϕ_0 (deg)	μ	$Gain_{peak}$ (dBi)	PSLL (dB)
0,0	0	28.48	-13.26
	0.257	28.34	-12.51
	0.39	28.32	-12.91
	0.5	28.12	-12.15
60,0 / 60,90	0	25.56 / 25.66	-11.44 / -11.7
	0.257	24.4 / 24.47	-9.42 / -10.37
	0.39	23.36 / 23.3	-8.81 / -9.73
	0.5	21.93 / 21.99	-7.17 / -6.25
60,45 / 60,225	0	25.44 / 25.75	-11.9 / -11.9
	0.257	24.39 / 24.75	-10.24 / -10.24
	0.39	23.29 / 23.68	-10.11 / -10.11
	0.5	21.94 / 22.37	-8.21 / -8.21

A. Practical Penrose Tiling Subarrays Design

With the aim of providing further experiment to assess the novel Penrose inspired partitioning scheme analytical approach correctness and investigate its robustness with respect to practical antenna elements aspect (such as mutual coupling), realistic radiating elements have been considered. Specifically, a coaxial cable fed patch antenna with a resonance frequency at 24 GHz has been chosen as array antenna element. A sketch of the patch antenna with its geometrical dimensions is depicted in Fig. 9a whereas the corresponding 16×16 triangular lattice array simulated by using Ansys HFSS [49], is shown in Fig. 9b. A Roger RO5880 substrate with a thickness of $h = 0.7$ mm and a dielectric constant of $\varepsilon_r = 2.2$ is adopted to support the patch.
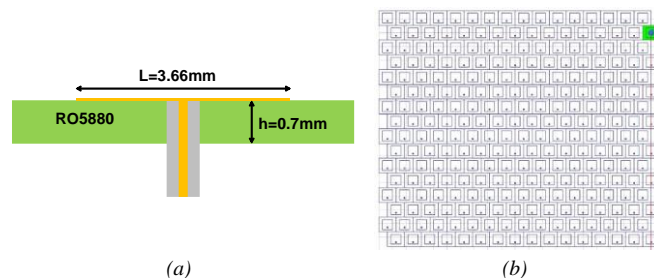

Fig. 9. (a) Side view of the array antenna element and (b) top view of the simulation model of the practical 16×16 array structure.

The normalized radiation pattern comparison between analytical model and full-wave simulation in case of 16×16 triangular lattice array evaluated for broadside direction ($\theta = 0°$) and 60° scan angle at $\phi = 90°$ plane are shown in Fig. 10 for different Penrose tiling tessellations with the corresponding array partitioning layouts depicted in Fig. 7l-n. This further experiments by considering realistic radiating elements, including mutual coupling effect, highlights the notable accuracy between the analytical model employed to estimate the radiation performance of the Penrose tiling subarrays and the full-wave simulations. This prove that the mutual coupling effect in the considered array structures is not significant due to the curves overlapping.
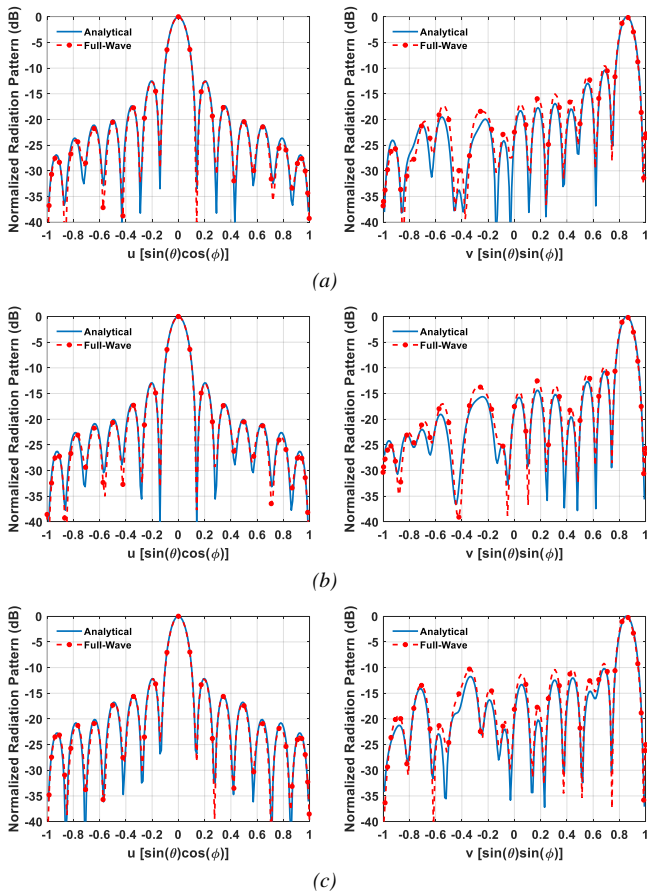
Fig. 10. Normalized radiation pattern comparison between results of the analytical model and full-wave simulation for a 16×16 triangular lattice array and Penrose tiling subarray for broadside scan (left column) and 60° scan angle at $\phi = 90°$ (right column): *(a)* $\mu = 0.257$ (190 feed points), *(b)* $\mu = 0.39$ (156 feed points) and *(c)* $\mu = 0.5$ (128 feed points).

As a further assessment of the proposed subarray design, although the array polarization (copolar and cross-polar) is highly dependent on the array element especially if all the array elements are oriented in the same direction [17] (as in this case), both copolar and cross polar component in case of Penrose subarray and FPA has been compared (Fig. 11). For brevity, just the Penrose tiling tessellations with $\mu = 0.39$ (156 feed points) and the array partitioning layouts depicted in Fig. 7*m* has been reported. Fig. 11 highlights a satisfactory agreement, especially around main beam direction (*i.e.* 60°) between the cross-polar components of the Penrose-inspired array and the FPA simulation. Specifically, when the array is steered along $\phi = 0°$ plane (Fig. 11*a*), namely the array E- plane, the cross-polar component undergoes a mild degradation in case of $\mu = 0.39$ (156 feed points) with respect to FPA, although it remains lower than 50 dB than copolar (60 dB in case of FPA). Conversely, during the main beam steering along $\phi = 90°$ plane (Fig. 11*b*), the cross-polar level is around 30 dB below the copolar one, as in the FPA case. Therefore, the Penrose partitioning scheme provides only a mild cross-polar degradation along array E-plane and hence, in general, it can be inferred that it does not considerably increase the cross-polar component.
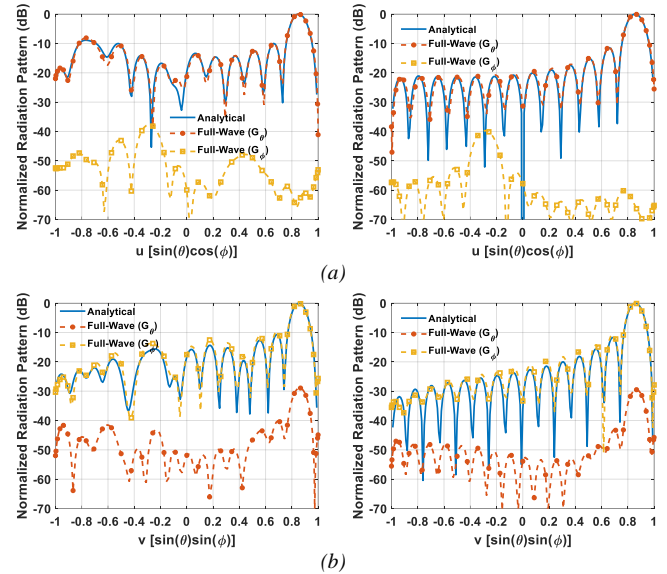

Fig. 11. Normalized radiation pattern comparison between results of the analytical model and full-wave simulation for a 16×16 triangular lattice array and Penrose tiling subarray with $\mu = 0.39$ (156 feed points) (left column) and FPA (right column): *(a)* 60° scan angle at $\phi = 0°$ and *(b)* 60° scan angle at $\phi = 90°$. Simulated results comprise both copolar and cross polar component.

IV. RECTANGULAR SCANNING AREA

In the previous section a large beam scanning within a circular area has been addressed. However, in some applications, such as ground base stations, automotive radars or aircraft landing systems, a wide beam scanning only in a principal plane (azimuth or elevation) is satisfactory. Therefore, the following analysis refers to a rectangular sector cell in the uv plane where the main beam can be steered with a 30° in elevation ($\pm15°$) and 120° ($\pm60°$) in azimuth. Moreover, an optimization on the two conflicting objectives of minimizing the thinning factor (μ) and the PSLL at maximum scan has been carried out to further emphasize the effectiveness as well as the versatility of the Penrose element clustering approach.

In this case, a raised cosine amplitude tapering has been applied at the subarrays level based on the distance from the array centre. The normalized amplitude $a(n,m)_r$ of all the element in the rth subarray turns out to be :

$$a(n,m)_r = t + (1-t)\cos\left(\frac{\pi d_r}{2d_{\max}}\right) \qquad (6)$$

where t represents the edge factor, d_r is the distance of the rth subarray centre from the array centre and d_{max} the maximum array length.

Fig. 12 displays the trade-off between two conflicting objectives through the Pareto front for different values of the Penrose triangle sides length L and edge taper of a 16×16 triangular lattice array with an inter element spacing of 0.5 λ_0. From the Pareto front of Fig. 12 it can be seen that different Penrose isosceles triangular sides length L determine a shifted Pareto curve. On the contrary, the raised cosine taper with $t > 0$ dB provides a down shift of the Pareto front with an improvement of the PSLL for the same thinning factor value. Moreover, the Pareto front related to the raised cosine taper

($t = 6$ dB) highlights as the amplitude tapering turns out to be more effective for low thinning factors. Conversely, the amplitude tapering effect on the PSLL lowering decreases more and more with the increasing the thinning factor (μ) due to a too accentuated staircase effect over the array aperture that badly approximate the cosine shape. Therefore, amplitude tapering in clustered arrays with large scanning angle helps mainly for low thinning factor values.
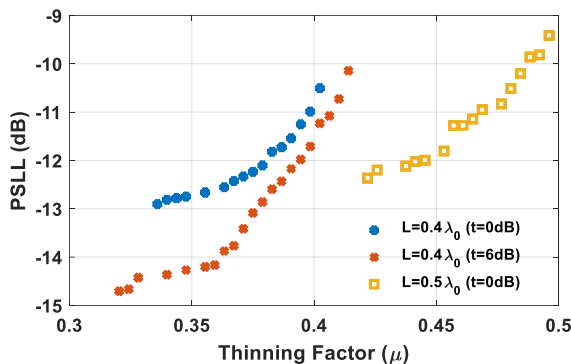

Fig. 12. Pareto front between PSLL and thinning factor (μ) for a rectangular scanning area of a $16{\times}16$ triangular lattice array by resorting to a raised cosine amplitude distribution at the subarrays level.

Among all the array partitions, the one with the lowest PSLL (*i.e.* -12.96 dB) in case of uniform amplitude distribution at the subarray level ($t = 0$dB) was considered.
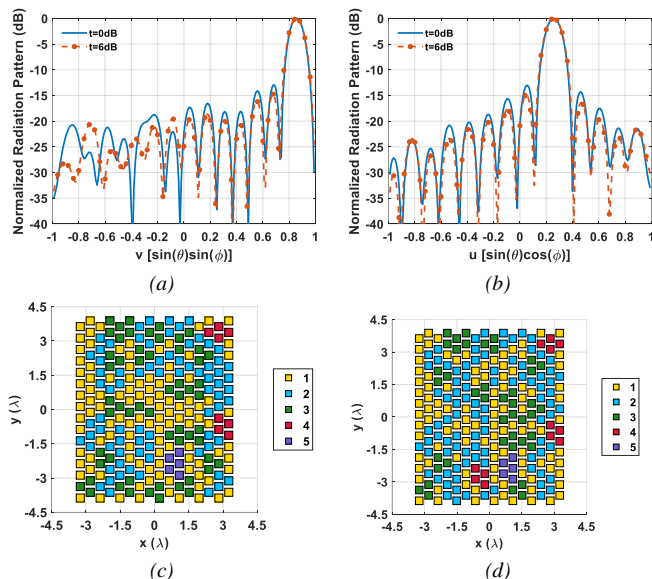

Fig. 13. Normalized radiation pattern with a $16{\times}16$ triangular lattice array and thinning factor of 0.33 (170 feed points): *(a)* $\phi = 90°$ plane with scan at $60°$ and *(b)* $\phi = 0°$ plane with scan at $15°$ *(c)* array layout with uniform amplitude ($t = 0$dB) and *(d)* array layout with amplitude tapering ($t = 6$dB).

The corresponding radiation patterns for a scan angle of $60°$ at $\phi = 90°$ plane and for a scan angle of $15°$ at $\phi = 0°$ plane are shown in Fig. 13*a-b*. For comparison, the radiation patterns with a raised cosine amplitude taper with an edge taper of 6 dB and the same thinning factor ($\mu = 0.33$) have been also reported. The related arrays partition layout in case of $\mu = 0.33$ with both uniform amplitude distribution ($t = 0$dB) and raised cosine

taper ($t = 6$ dB) are depicted in Fig. 13*c-d*. The main amplitude tapering effect is to slightly reduce the lateral lobes near the main beam whereas its effect fades little by little for those farther away.

To provide a general overview regarding the radiative performance of the selected partitions highlighted in Fig. 13*c-d*, the peak gain and the PSLL are shown in Fig. 14 as a function of the main beam direction inside the rectangular sector cell. As it is evident, although a feeding points reduction of 33%, the Penrose clustered arrays continue to have a meaningful control capability of the radiation by allowing a consistent PSLL lowering in addiction to a noteworthy array gain value as a function of the main beam direction (Fig. 14). In particular, the uniform amplitude distribution at the subarrays level (Fig. 14*a*) is able to maintain the PSLL at around -13 dB also for large scanning angles. Conversely, the edge taper of 6 dB (Fig. 14*b*) allows a significant PSLL lowering around the broadside direction (lower than -15 dB) and maintain a value lower than -14 dB at the edge of the scanning.

It is worth underlining that, in case of a FPA and uniform amplitude distribution, the radiation at the edges of the rectangular scanning area is characterized by a PSLL of -11.7 dB. By resorting to the Penrose tiling subarrays technology, the same PSLL of -11.7 dB, can be achieved with a $\mu = 0.386$ (157 feed points) for $L = 0.4 \, \lambda_0$ and with a $\mu = 0.45$ (140 feed points) for $L = 0.5 \, \lambda_0$ (Fig. 12).
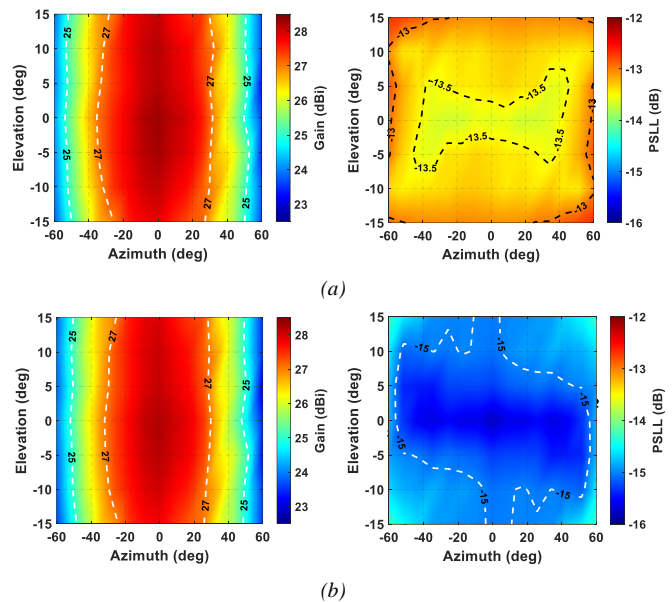

Fig. 14. Color maps highlighting the array gain and the PSLL as a function of the main beam direction inside the rectangular sector of a $16{\times}16$ triangular lattice array with a thinning factor of 0.33 (170 feed points) in case of *(a)* uniform amplitude ($t = 0$ dB) and *(b)* raised cosine amplitude distribution with edge taper equal to 6 dB.

The arrays layout and the associated radiation patterns able to provide a maximum PSLL on the rectangular cell of -11.7 dB are reported in Fig. 15. As previously remarked, even though the clustered arrays can provide the same PSLL of FPA ($\mu = 0$), they produce a larger spreading energy over the visible region caused by higher lateral lobes with a consequent peak gain

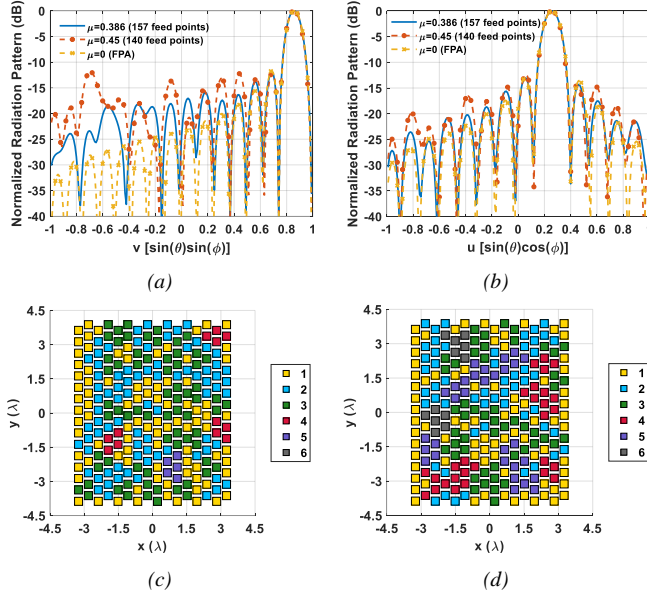reduction. In general, the lower is the number of available feed points, the greater is the energy spreading.

Fig. 15. Normalized radiation pattern with a 16×16 triangular lattice array in case of different thinning factor values for *(a)* $\phi = 90°$ plane with scan at 60° and *(b)* $\phi = 0°$ plane with scan at 15° *(c)* array layout with $\mu = 0.386$ (157 feed point) and *(d)* array layout with $\mu = 0.45$ (140 feed points).

A. Practical Penrose Tiling Subarrays Design

Similarly to the previous section, the radiative performance of the Penrose tiling subarrays have been validated by considering realistic radiating elements also in case of a beam scanning within a rectangular area. Thereby, the considered patch antenna element and the 16×16 triangular lattice array shown in Fig. 9 has been adopted for the full-wave simulations.

Fig. 16 shows the normalized radiation pattern comparison between analytical model and simulation for two scan angles within the predefined rectangular sector in case of uniform amplitude distribution at the subarray level and thinning factor of 0.33 (Fig. 16*a*) and then with a raised cosine amplitude taper with an edge taper of 6 dB and the same thinning (Fig. 16*b*). Specifically, the curves refer to two different array partition layouts previously shown in Fig. 13*c-d*. By looking at Fig. 16 it is apparent that the analytical approach and the simulation one present a satisfactory agreement both around the main beam lobe and for the lateral lobes which confirms the reliability of the Penrose partitioning scheme and the negligible effect of mutual coupling among antenna elements.

For the sake of completeness, the radiation patterns comparison has been carried out also by considering the array partitioning layouts shown in Fig. 15*c-d*, namely with a $\mu = 0.386$ (157 feed points) and with a $\mu = 0.45$ (140 feed points), where the same considerations can be derived (Fig. 17).

V. UNBALANCED FEEDING EFFECT

So far, the previous radiative performance were obtained by considering an ideal feeding for all the array antenna elements. However, real-life scenario is facing numerous non-ideality such as manufacturing errors, electronic inaccuracies and

TRMs unbalances that lead to some alterations of both amplitude and phase of array antenna elements feeding.
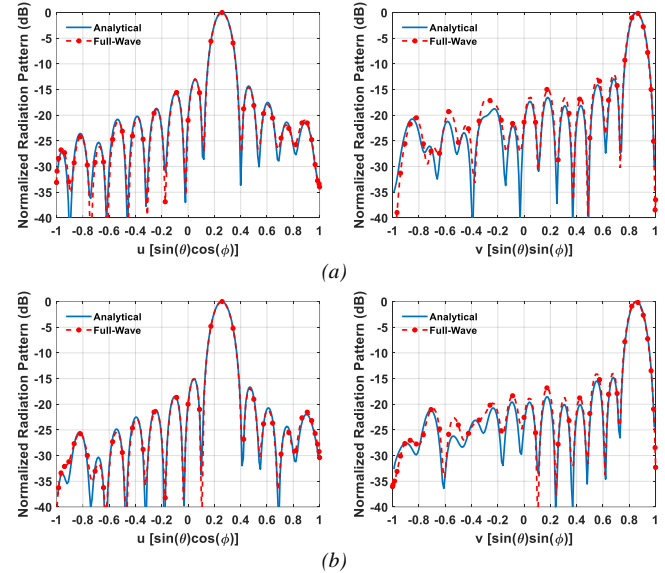

Fig. 16. Normalized radiation pattern comparison between results of the analytical model and full-wave simulations for a 16×16 triangular lattice array and Penrose tiling subarray in case of $\mu = 0.33$ (170 feed points) for scan angle of 15° at $\phi = 0°$ plane (left column) and 60° scan angle at $\phi = 90°$ (right column): *(a)* uniform amplitude ($t = 0$dB) with array layout shown in Fig. 13*c* and *(b)* raised cosine amplitude tapering ($t = 6$ dB) with array partition depicted in Fig. 13*d*.
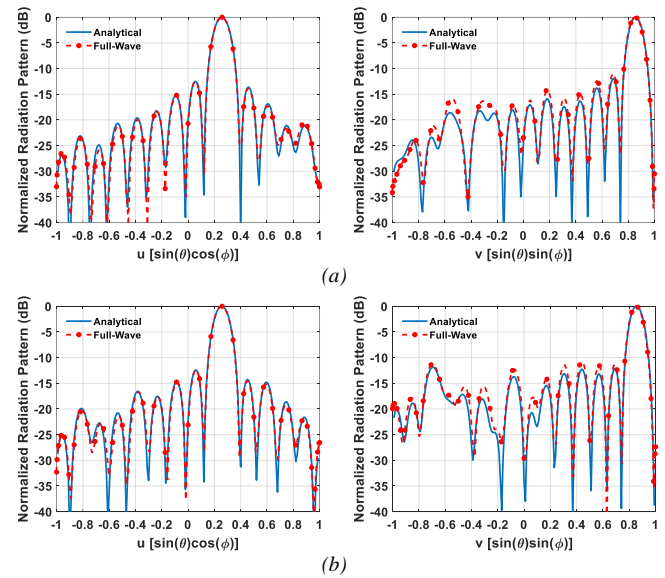
Fig. 17. Normalized radiation pattern comparison between results of the analytical model and full-wave simulation for a 16×16 triangular lattice array and Penrose tiling subarray in case of uniform amplitude ($t = 0$dB) for scan angle of 15° at $\phi = 0°$ plane (left column) and 60° scan angle at $\phi = 90°$ (right column): *(a)* $\mu = 0.386$ (157 feed points) with array layout shown in Fig. 15*c* and *(b)* $\mu = 0.45$ (140 feed points) and array layout depicted in Fig. 15*d*.

To cope with these inaccuracies that inevitably degrade the beamforming quality and hence the link data rate, it is common to perform the phased array calibration. However, it represents one of the main array costs and hence its usage must be accurately assessed by making a sort of trade-off between the overall cost and the performance needs [50].

Fig. 18. Normalized radiation pattern in case of 16×16 triangular lattice array and a Penrose partitioning scheme with random ±2 dB amplitude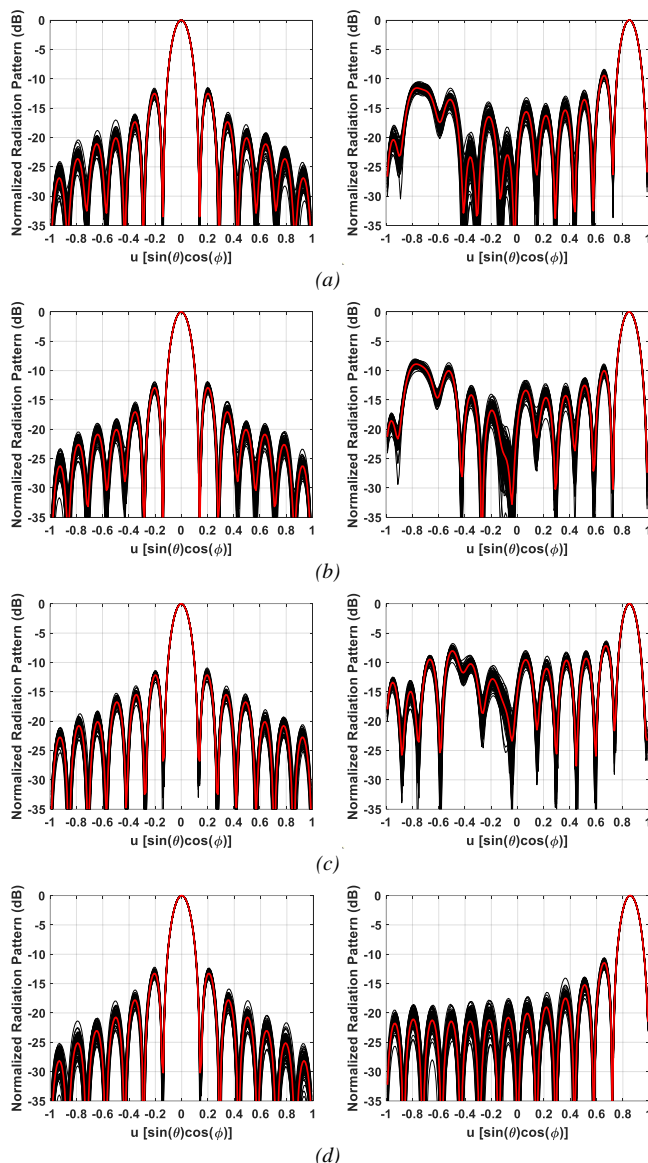 and ±20° feeding error for broadside scan (left column) and 60° scan angle at $\phi = 0°$ (right column): (a) $\mu = 0.257$ (190 feed points), (b) $\mu = 0.39$ (156 feed points), (c) $\mu = 0.5$ (128 feed points) and (d) FPA (256 feed points).

To highlight the performance impairment due to the lack of calibration procedure or its degradation due to the change of environment conditions, the Penrose partitioning scheme radiative performance were evaluated in case of random errors applied to the ideal feeding to steer the main beam. More in detail, as a proof of concept, a random unbalanced of ±2 dB amplitude and ±20° feeding error was applied to all array radiative element. Fig. 18 presents the normalized radiation pattern for a 16×16 triangular lattice array for two scan angles by considering 100 random unbalanced feeding profiles (black curves) and the ideal one (red curve). Specifically, Fig. 18a-c refers to three Penrose partition layouts previously shown in Fig. 7l-n with different thinning factor, whereas in Fig. 18d the FPA case for comparison is reported. For brevity, the effect of unbalanced feeding on the radiation pattern for the other

investigated Penrose partitioning schemes have not been reported.

As it is evident from Fig. 18, the unbalanced feeding slightly affects the radiation pattern by increasing or decreasing lateral lobes but, in general, its impact turns out somewhat negligible around the main beam by leading to a mild alteration of the array gain. Moreover, the mild changes exhibited by a Penrose-tiled array are comparable to those suffered by a FPA one (Fig. 18d).

VI. POWER CONSUMPTION ANALYSIS

It has been proved that the Penrose subarrays tiling can guarantee a remarkable TRM reduction thus decreasing both the hardware cost and complexity of a phased array without severely compromising the overall performance. However, power consumption has to be considered as well, since it plays a key role in the evolution of the phased arrays.

It is apparent that to achieve the same Equivalent Isotropic Radiated Power (EIRP) of a FPA, the PA associated to each subarray has to provide a higher output power. This aspect, if not accurately considered, can pose significant challenges at system level. One of these issues lies in the PA nonlinearities that can affect the Error Vector Module (EVM) or the Adjacent Channel Power Ratio (ACPR), namely the modulation error of the signal with respect to the reference constellation and the interference toward users operating in the adjacent channels, respectively [51]. Specifically, each PA of the partitioned array has to guarantee an output power ($P_o{}^{SA}$) expressed in dB$_w$ equal to:

$$P_o^{SA}\left(\theta_0,\phi_0\right) = P_o^{FPA} + 10\log_{10}\left(\frac{1}{1-\mu}\right) + G_{diff}\left(\theta_0,\phi_0\right) \qquad (7)$$

where $P_o{}^{FPA}$ represents the PA output power *per element* in case of a FPA, μ is the thinning factor whereas $G_{diff}(\theta_0,\phi_0)$ expresses the difference in dB between the FPA gain (G_{FPA}) and the partitioned one (G_{SA}) along the main beam direction (θ_0,ϕ_0). The power per PA, required to preserve the same EIRP of a FPA, is strongly dependent from the number of subarrays and the arrays gain difference.

For the total power consumption (P_{total}) assessment it is necessary to know the phased array architecture. Fig. 19 illustrates a typical architecture for a hybrid beamforming phased array.
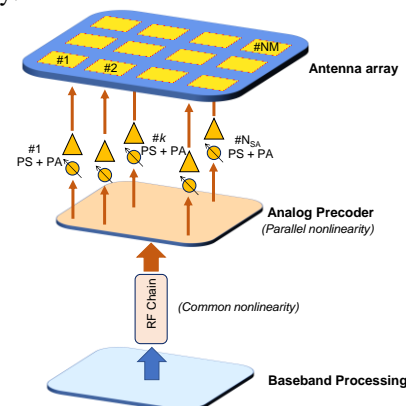

Fig. 19. Block diagram of the transmitter architecture of an active electronically beam scanning antenna.

The Radio Frequency Chain (RFC) is connected to the antenna array equipped by ($N \times M$) elements through the analog precoder composed by N_{SA} Phase Shifters (PSs) and PAs. A similar model can be derived for the receiver by replacing the PAs with Low Noise Amplifiers (LNAs). Fig. 19 also highlights the source of nonlinearity of a phased array. Common nonlinearity that occurs in the RFC does not change the beam shape. On the contrary, the parallel nonlinearity due to different PS and PA for each branch can substantially alter the radiation performance. Given the block diagram of Fig. 19, the total power consumption (P_{tot}) can be evaluated as:

$$P_{tot} = P_{BB} + P_{RFC} + N_{SA}P_{PS} + N_{SA}\frac{\left(P_o^{SA} - P_i^{SA}\right)}{\eta_{SA}} \qquad (8)$$

where N_{SA} denotes the number of subarrays (feed points) whereas, P_{RFC}, P_{PS} and P_{BB}, the power consumption of the RFC, PS and baseband processing respectively. The ratio $(P_o^{SA} - P_i^{SA})/\eta_{SA}$, where P_o^{SA}, P_i^{SA} and η_{SA} indicates the PA output power, input power and Power Added Efficiency (PAE) respectively, models the PA power consumption. Located in the middle between the antenna array and the transceiver, PA represents a crucial component of the system that governs many performance aspects of the wireless link, including the total power consumption. Given a phased array architecture with a clustered array, the general condition that allows obtaining a lowering of P_{tot} with respect to the FPA is:

$$\frac{\left(P_o^{SA} - P_i^{SA}\right)}{\eta_{SA}} \le \frac{1}{1-\mu}\left[P_{PS} + \frac{\left(P_o^{FPA} - P_i^{FPA}\right)}{\eta_{FPA}}\right] - P_{PS} \qquad (9)$$

where the ratio $(P_o^{FPA} - P_i^{FPA})/\eta_{FPA}$ refers to the power consumption of single PA in case of FPA. Hence, under the hypothesis that $P_o^{SA} \gg P_i^{SA}$ and $P_o^{FPA} \gg P_i^{FPA}$ the conditions on PAE of PAs capable of providing energy-saving clustered phased array is:

$$\eta_{SA} > \frac{P_o^{FPA}}{\dfrac{G_{SA}}{G_{FPA}}\left[\mu P_{PS} + \dfrac{P_o^{FPA}}{\eta_{FPA}}\right]} \qquad (10)$$

Equation (10) shows that to allows a lower P_{tot} the operating point of the PAs in case of clustered array has to guarantee a η_{SA} certainly higher than η_{FPA}. In particular, the minimum value of η_{SA} is strongly affected by the arrays gain ratio (G_{SA}/G_{FPA}) evaluated at the same main beam direction (θ_0, ϕ_0), phased array thinning factor (μ) and the PS power consumption (P_{PS}). Therefore, equations (7) and (10) summarize the PA requirements to achieve an energy-efficient phased array in terms of output power (P_o^{SA}) expressed in dB$_w$ and the PAE, respectively. It is worth noting that (7) and (9)-(10) allow reducing the total power consumption (P_{tot}) with respect to FPA under the assumption of the same EIRP value as well as equal PA characteristics.

As a proof of concept, the commercial PA (APM-6848SM) based on GaAs HBT technology and capable of providing a saturated power (P_{sat}) of 21 dBm has been used for the power consumption (P_{total}) assessment. The PA characteristics in terms of output power (P_o) and PAE as a function of the input power (P_i) is reported in Fig. 20. The PA conditions for an energy-saving phased array are reported in Fig. 21 as a function of the main beam direction by assuming an EIRP of 65 dBm and a Penrose tiling subarray architecture with a $\mu = 0.39$ (156 feed points) with an array layout as in Fig. 7m. More in detail, Fig. 21a highlights the minimum PAE by exploiting (10) whereas the back-off (BO) value, namely the output power level below the saturated one of 21 dBm, is reported in Fig. 21b by considering an output power (P_o^{SA}) given by (7). As it is evident, the necessary conditions of the PAs present a somewhat small PAE and output power ($\eta_{SA} < 6\%$ and $BO > 5$ dB) for limited scan angles. However, with the increasing of the steering angle, BO become lower and lower up to reaches $BO < 3$ dB for steering angles greater than 50° whereas the necessary PAE can require values greater than 10 %.
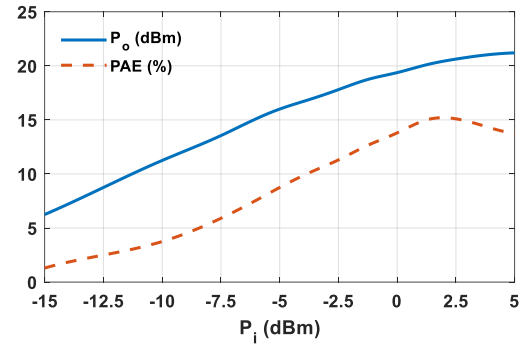

Fig. 20. Power amplifier (APM-6848SM) characteristics as a function of the input power.
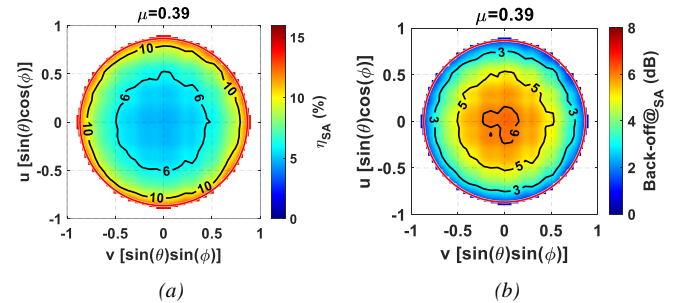
Fig. 21. Power amplifier conditions on (a) PAE and (b) BO for an energy-saving clustered array as a function of the main beam direction to achieve an EIRP of 65 dBm in case of a 16×16 triangular lattice array with a thinning factor of 0.39 (156 feed points) for the array partition shown in Fig. 7m.

Fig. 22 shows the total power consumption (P_{tot}) with respect to the main beam direction by considering the commercial PA (APM-6848SM) in case of a 16×16 triangular lattice array based on a Penrose tiling subarray architecture with $\mu = 0.39$ (156 feed points) and the array partition shown in Fig. 7m. Specifically, a power consumption of $P_{PS} = 50$ mW, $P_{BB} = 200$ mW and $P_{RFC} = 1.27$ W has been adopted for the P_{tot} evaluation. Moreover, the line contours illustrated in the color maps of Fig. 22 highlight the percentage reduction of the power consumption with respect to the 16×16 triangular lattice FPA. It can be drawn that, the PA model APM-6848SM is able to satisfy the previous requirements (Fig. 21) in terms of PAE and P_o^{SA} since the P_{tot} undergoes a significantly reduction, especially around broadside direction. Specifically, an energy

This article has been accepted for publication in IEEE Transactions on Antennas and Propagation. This is the author's version which has not been fully edited and content may change prior to final publication. Citation information: DOI 10.1109/TAP.2022.3178917

> REPLACE THIS LINE WITH YOUR PAPER IDENTIFICATION NUMBER (DOUBLE-CLICK HERE TO EDIT) <   12

saving greater than 30 % occurs for steering angles lower than 15 , then it gently decreases with the increasing of the main beam direction but preserving a considerable power reduction. It is worth pointing out that, the attained percentage power reduction shown in Fig. 22 cannot be generalized because it is dependent on the selected EIRP value, the PS power consumption (P_{PS}) and the adopted clustered array configuration (μ).

In general, the selection of a PA occurs in such a way, with the correspond output power per element able to achieve the desired EIRP, the selected PA works at a certain amount of back-off level in order to have a reasonable PAE level but, at the same time, to preserve the transceiver linearity.
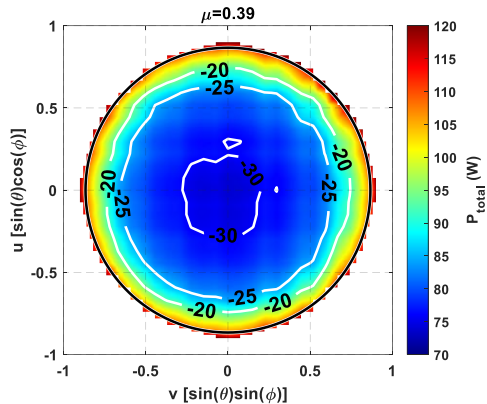

Fig. 22. Total power consumption (P_{tot}) as a function of the main beam direction by considering the PA model APM-6848SM to achieve an EIRP of 65 dBm in case of a 16×16 triangular lattice array based on a Penrose tiling subarray with $\mu = 0.39$ (156 feed points) and the array partition shown in Fig. 7m. Contour lines report the percentage reduction of the power consumption with respect to the 16×16 triangular lattice FPA.

However, in the clustered array architecture the output power of each PA (P_o^{SA}) has to be increased of a certain amount (7) to preserve the EIRP in order to compensate for a TRMs reduction. As a result, the PA able to work at a lower back-off power level, as well as improving the PAE, may introduce more nonlinearity effects to the system. It is therefore necessary to verify for each particular case if the related transceiver distortion is compliant with the systems requirements. A suitable trade-off between the reduction of cost and complexity and PA operation point in terms of BO level may be requested. It is important to mention that some linearization techniques such as the Digital Predistortion (DPD) [52] can be successfully adopted to maintain the transceiver linearity even in the illustrated scenario. Another alternative is represented by the selection of different PAs that can satisfy both the energy-efficient requirements and the linearity [53], [54] as well as the adoption of variable PAs biasing control according to the input power level to improve their PAE [55].

VII. CONCLUSION

A novel subarray partitioning scheme based on Penrose tessellation has been proposed for wide-scan phased array. The original fully populated array with elements arranged in a triangular lattice has been organized into irregularly-shaped tiles that allow a noteworthy reduction of the Transmit/Receive modules by exploiting the aperiodic Penrose tiling. This simplification of the architecture has been achieved without compromising the performance in terms of scan angle and peak side lobe level thanks to a design process based on the Pareto front optimization. The novel array paradigm based on Penrose-inspired subarrays has been tested for both circular and rectangular scan areas and it has proved to guarantee the desired performance in terms of angular coverage and sidelobe level even with the less complex RF fronted.

Moreover, an extensive analysis regarding the power consumption and the requirements for energy-saving clustered phased arrays with respect to the FPA one is addressed under the hypothesis of the same EIRP value as well as equal characteristics of the chosen PAs in terms of output power (P_o) and PAE as a function of the input power (P_i).

The simulated analysis based on a commercial PA, an EIRP of 65 dBm and a feeding points reduction of 39% proved a significantly power consumption reduction with respect to a FPA, especially around broadside direction, as well as the preservation of a meaningful control capability of the radiative performance.

REFERENCES

[1] W. Hong *et al.*, 'Multibeam Antenna Technologies for 5G Wireless Communications', *IEEE Trans. Antennas Propag.*, vol. 65, no. 12, pp. 6231–6249, Dec. 2017, doi: 10.1109/TAP.2017.2712819.

[2] E. Björnson, J. Hoydis, and L. Sanguinetti, 'Massive MIMO Networks: Spectral, Energy, and Hardware Efficiency', *Found. Trends® Signal Process.*, vol. 11, no. 3–4, pp. 154–655, 2017, doi: 10.1561/2000000093.

[3] F. A. Dicandia, S. Genovesi, and A. Monorchio, 'Analysis of the Performance Enhancement of MIMO Systems Employing Circular Polarization', *IEEE Trans. Antennas Propag.*, vol. 65, no. 9, pp. 4824–4835, Sep. 2017, doi: 10.1109/TAP.2017.2723083.

[4] E. Björnson, L. Sanguinetti, J. Hoydis, and M. Debbah, 'Optimal Design of Energy-Efficient Multi-User MIMO Systems: Is Massive MIMO the Answer?', *IEEE Trans. Wirel. Commun.*, vol. 14, no. 6, pp. 3059–3075, Jun. 2015, doi: 10.1109/TWC.2015.2400437.

[5] P. M. Asbeck, N. Rostomyan, M. Özen, B. Rabet, and J. A. Jayamon, 'Power Amplifiers for mm-Wave 5G Applications: Technology Comparisons and CMOS-SOI Demonstration Circuits', *IEEE Trans. Microw. Theory Tech.*, vol. 67, no. 7, pp. 3099–3109, Jul. 2019, doi: 10.1109/TMTT.2019.2896047.

[6] Y. Aslan, J. Puskely, J. H. J. Janssen, M. Geurts, A. Roederer, and A. Yarovoy, 'Thermal-Aware Synthesis of 5G Base Station Antenna Arrays: An Overview and a Sparsity-Based Approach', *IEEE Access*, vol. 6, pp. 58868–58882, 2018, doi: 10.1109/ACCESS.2018.2873977.

[7] J. S. Herd and M. D. Conway, 'The Evolution to Modern Phased Array Architectures', *Proc. IEEE*, vol. 104, no. 3, pp. 519–529, Mar. 2016, doi: 10.1109/JPROC.2015.2494879.

[8] P. Rocca, G. Oliveri, R. J. Mailloux, and A. Massa, 'Unconventional Phased Array Architectures and Design Methodologies—A Review', *Proc. IEEE*, vol. 104, no. 3, pp. 544–560, Mar. 2016, doi: 10.1109/JPROC.2015.2512389.

[9] Y. Aslan, A. Roederer, and A. Yarovoy, 'System Advantages of Using Large-Scale Aperiodic Array Topologies in Future mm-Wave 5G/6G Base Stations: An Interdisciplinary Look', *IEEE Syst. J.*, pp. 1–10, 2021, doi: 10.1109/JSYST.2020.3045909.

[10] D. Bianchi, S. Genovesi, and A. Monorchio, 'Constrained Pareto Optimization of Wide Band and Steerable Concentric Ring Arrays', *IEEE Trans. Antennas Propag.*, vol. 60, no. 7, pp. 3195–3204, Jul. 2012, doi: 10.1109/TAP.2012.2196909.

[11] O. M. Bucci, M. D'Urso, T. Isernia, P. Angeletti, and G. Toso, 'Deterministic Synthesis of Uniform Amplitude Sparse Arrays via New Density Taper Techniques', *IEEE Trans. Antennas Propag.*, vol. 58, no. 6, pp. 1949–1958, Jun. 2010, doi: 10.1109/TAP.2010.2046831.

This article has been accepted for publication in IEEE Transactions on Antennas and Propagation. This is the author's version which has not been fully edited and content may change prior to final publication. Citation information: DOI 10.1109/TAP.2022.3178917

> REPLACE THIS LINE WITH YOUR PAPER IDENTIFICATION NUMBER (DOUBLE-CLICK HERE TO EDIT) <   13

[12] R. L. Haupt, 'Thinned arrays using genetic algorithms', *IEEE Trans. Antennas Propag.*, vol. 42, no. 7, pp. 993–999, Jul. 1994, doi: 10.1109/8.299602.

[13] W. P. M. N. Keizer, 'Synthesis of Thinned Planar Circular and Square Arrays Using Density Tapering', *IEEE Trans. Antennas Propag.*, vol. 62, no. 4, pp. 1555–1563, Apr. 2014, doi: 10.1109/TAP.2013.2267194.

[14] R. L. Haupt, 'Adaptively Thinned Arrays', *IEEE Trans. Antennas Propag.*, vol. 63, no. 4, pp. 1626–1632, Apr. 2015, doi: 10.1109/TAP.2015.2394785.

[15] Y. Aslan, J. Puskely, A. Roederer, and A. Yarovoy, 'Trade-offs between the quality of service, computational cost and cooling complexity in interference-dominated multi-user SDMA systems', *IET Commun.*, vol. 14, no. 1, pp. 144–151, Jan. 2020, doi: 10.1049/iet-com.2019.0206.

[16] Y. Aslan, J. Puskely, A. Roederer, and A. Yarovoy, 'Multiple Beam Synthesis of Passively Cooled 5G Planar Arrays Using Convex Optimization', *IEEE Trans. Antennas Propag.*, vol. 68, no. 5, pp. 3557–3566, May 2020, doi: 10.1109/TAP.2019.2955885.

[17] R. L. Haupt, *Antenna arrays: a computational approach*. Hoboken, N.J: Wiley-IEEE Press, 2010.

[18] H. M. Aumann, A. J. Fenn, and F. G. Willwerth, 'Phased array antenna calibration and pattern prediction using mutual coupling measurements', *IEEE Trans. Antennas Propag.*, vol. 37, no. 7, pp. 844–850, Jul. 1989, doi: 10.1109/8.29378.

[19] A. Nafe, K. Kibaroglu, M. Sayginer, and G. M. Rebeiz, 'An In-Situ Self-Test and Self-Calibration Technique Utilizing Antenna Mutual Coupling for 5G Multi-Beam TRX Phased Arrays', in *2019 IEEE MTT-S International Microwave Symposium (IMS)*, Jun. 2019, pp. 1229–1232. doi: 10.1109/MWSYM.2019.8701072.

[20] P. Rocca, N. Anselmi, A. Polo, and A. Massa, 'Modular Design of Hexagonal Phased Arrays Through Diamond Tiles', *IEEE Trans. Antennas Propag.*, vol. 68, no. 5, pp. 3598–3612, May 2020, doi: 10.1109/TAP.2019.2963561.

[21] T. Azar, 'Overlapped Subarrays: Review and Update [Education Column]', *IEEE Antennas Propag. Mag.*, vol. 55, no. 2, pp. 228–234, Apr. 2013, doi: 10.1109/MAP.2013.6529353.

[22] D. Bianchi, S. Genovesi, and A. Monorchio, 'Randomly Overlapped Subarrays for Reduced Sidelobes in Angle-Limited Scan Arrays', *IEEE Antennas Wirel. Propag. Lett.*, vol. 16, pp. 1969–1972, 2017, doi: 10.1109/LAWP.2017.2690824.

[23] B. Avser, J. Pierro, and G. M. Rebeiz, 'Random Feeding Networks for Reducing the Number of Phase Shifters in Limited-Scan Arrays', *IEEE Trans. Antennas Propag.*, vol. 64, no. 11, pp. 4648–4658, Nov. 2016, doi: 10.1109/TAP.2016.2600861.

[24] P. Rocca, R. J. Mailloux, and G. Toso, 'GA-Based Optimization of Irregular Subarray Layouts for Wideband Phased Arrays Design', *IEEE Antennas Wirel. Propag. Lett.*, vol. 14, pp. 131–134, 2015, doi: 10.1109/LAWP.2014.2356855.

[25] R. J. Mailloux, S. G. Santarelli, T. M. Roberts, and D. Luu, 'Irregular Polyomino-Shaped Subarrays for Space-Based Active Arrays', *Int. J. Antennas Propag.*, vol. 2009, pp. 1–9, 2009, doi: 10.1155/2009/956524.

[26] Y. Ma, S. Yang, Y. Chen, S.-W. Qu, and J. Hu, 'Pattern Synthesis of 4-D Irregular Antenna Arrays Based on Maximum-Entropy Model', *IEEE Trans. Antennas Propag.*, vol. 67, no. 5, pp. 3048–3057, May 2019, doi: 10.1109/TAP.2019.2896730.

[27] Y. Ma, S. Yang, Y. Chen, S. Qu, and J. Hu, 'High Directivity Optimization Technique for Irregular Arrays Combined with Maximum Entropy Model', *IEEE Trans. Antennas Propag.*, pp. 1–1, 2020, doi: 10.1109/TAP.2020.3044653.

[28] F. A. Dicandia and S. Genovesi, 'Exploitation of Triangular Lattice Arrays for Improved Spectral Efficiency in Massive MIMO 5G Systems', *IEEE Access*, vol. 9, pp. 17530–17543, 2021, doi: 10.1109/ACCESS.2021.3053091.

[29] F. A. Dicandia and S. Genovesi, 'Spectral Efficiency Improvement of 5G Massive MIMO Systems for High-Altitude Platform Stations by Using Triangular Lattice Arrays', *Sensors*, vol. 21, no. 9, p. 3202, May 2021, doi: 10.3390/s21093202.

[30] J. Ala-Laurinaho *et al.*, '2-D Beam-Steerable Integrated Lens Antenna System for 5G E-Band Access and Backhaul', *IEEE Trans. Microw. Theory Tech.*, vol. 64, no. 7, pp. 2244–2255, Jul. 2016, doi: 10.1109/TMTT.2016.2574317.

[31] B. Rupakula, A. H. Aljuhani, and G. M. Rebeiz, 'Limited Scan-Angle Phased Arrays Using Randomly Grouped Subarrays and Reduced Number of Phase Shifters', *IEEE Trans. Antennas Propag.*, vol. 68, no. 1, pp. 70–80, Jan. 2020, doi: 10.1109/TAP.2019.2935100.

[32] A. Konak, D. W. Coit, and A. E. Smith, 'Multi-objective optimization using genetic algorithms: A tutorial', *Reliab. Eng. Syst. Saf.*, vol. 91, no. 9, pp. 992–1007, Sep. 2006, doi: 10.1016/j.ress.2005.11.018.

[33] T. Isernia, M. D'Urso, and O. M. Bucci, 'A Simple Idea for an Effective Sub-Arraying of Large Planar Sources', *IEEE Antennas Wirel. Propag. Lett.*, vol. 8, pp. 169–172, 2009, doi: 10.1109/LAWP.2008.2000943.

[34] V. Pierro, V. Galdi, G. Castaldi, I. M. Pinto, and L. B. Felsen, 'Radiation properties of planar antenna arrays based on certain categories of aperiodic tilings', *IEEE Trans. Antennas Propag.*, vol. 53, no. 2, pp. 635–644, Feb. 2005, doi: 10.1109/TAP.2004.841287.

[35] T. G. Spence and D. H. Werner, 'Design of Broadband Planar Arrays Based on the Optimization of Aperiodic Tilings', *IEEE Trans. Antennas Propag.*, vol. 56, no. 1, pp. 76–86, Jan. 2008, doi: 10.1109/TAP.2007.913145.

[36] U. Siddique, H. Tabassum, E. Hossain, and D. I. Kim, 'Wireless backhauling of 5G small cells: challenges and solution approaches', *IEEE Wirel. Commun.*, vol. 22, no. 5, pp. 22–31, Oct. 2015, doi: 10.1109/MWC.2015.7306534.

[37] F. A. Dicandia and S. Genovesi, 'A Compact CubeSat Antenna With Beamsteering Capability and Polarization Agility: Characteristic Modes Theory for Breakthrough Antenna Design', *IEEE Antennas Propag. Mag.*, vol. 62, no. 4, pp. 82–93, Aug. 2020, doi: 10.1109/MAP.2020.2965015.

[38] F. A. Dicandia and S. Genovesi, 'Characteristic Modes Analysis of Non-Uniform Metasurface Superstrate for Nanosatellite Antenna Design', *IEEE Access*, vol. 8, pp. 176050–176061, 2020, doi: 10.1109/ACCESS.2020.3027251.

[39] C. Liu, S. Xiao, H. Tu, and Z. Ding, 'Wide-Angle Scanning Low Profile Phased Array Antenna Based on a Novel Magnetic Dipole', *IEEE Trans. Antennas Propag.*, vol. 65, no. 3, pp. 1151–1162, Mar. 2017, doi: 10.1109/TAP.2016.2647711.

[40] F. A. Dicandia, S. Genovesi, and A. Monorchio, 'Efficient Excitation of Characteristic Modes for Radiation Pattern Control by Using a Novel Balanced Inductive Coupling Element', *IEEE Trans. Antennas Propag.*, vol. 66, no. 3, pp. 1102–1113, Mar. 2018, doi: 10.1109/TAP.2018.2790046.

[41] Y.-Y. Bai, S. Xiao, M.-C. Tang, Z.-F. Ding, and B.-Z. Wang, 'Wide-Angle Scanning Phased Array With Pattern Reconfigurable Elements', *IEEE Trans. Antennas Propag.*, vol. 59, no. 11, pp. 4071–4076, Nov. 2011, doi: 10.1109/TAP.2011.2164176.

[42] Y. Kim, H. Dong, K. Kim, and H. L. Lee, 'Compact Planar Multipole Antenna for Scalable Wide Beamwidth and Bandwidth Characteristics', *IEEE Trans. Antennas Propag.*, vol. 68, no. 5, pp. 3433–3442, May 2020, doi: 10.1109/TAP.2020.2963925.

[43] J. Ignacio Echeveste, M. Á. González de Aza, J. Rubio, and C. Craeye, 'Gradient-Based Aperiodic Array Synthesis of Real Arrays With Uniform Amplitude Excitation Including Mutual Coupling', *IEEE Trans. Antennas Propag.*, vol. 65, no. 2, pp. 541–551, Feb. 2017, doi: 10.1109/TAP.2016.2638359.

[44] H. V. Bui, S. N. Jha, and C. Craeye, 'Fast Full-Wave Synthesis of Printed Antenna Arrays Including Mutual Coupling', *IEEE Trans. Antennas Propag.*, vol. 64, no. 12, pp. 5163–5171, Dec. 2016, doi: 10.1109/TAP.2016.2617778.

[45] C. Bencivenni, M. V. Ivashina, R. Maaskant, and J. Wettergren, 'Design of Maximally Sparse Antenna Arrays in the Presence of Mutual Coupling', *IEEE Antennas Wirel. Propag. Lett.*, vol. 14, pp. 159–162, 2015, doi: 10.1109/LAWP.2014.2357450.

[46] 'MATLAB'. https://it.mathworks.com/products/matlab.html (accessed Jun. 17, 2021).

[47] B. Sadhu *et al.*, 'A 28-GHz 32-Element TRX Phased-Array IC With Concurrent Dual-Polarized Operation and Orthogonal Phase and Gain Control for 5G Communications', *IEEE J. Solid-State Circuits*, vol. 52, no. 12, pp. 3373–3391, Dec. 2017, doi: 10.1109/JSSC.2017.2766211.

[48] N. Tervo, M. E. Leinonen, J. Aikio, T. Rahkonen, and A. Pärssinen, 'Analyzing the Effects of PA Variations on the Performance of Phased Array Digital Predistortion', in *2018 IEEE 29th Annual International Symposium on Personal, Indoor and Mobile Radio Communications (PIMRC)*, Sep. 2018, pp. 215–219. doi: 10.1109/PIMRC.2018.8580706.

[49] 'Ansys HFSS | 3D High Frequency Simulation Software'. https://www.ansys.com/it-it/products/electronics/ansys-hfss (accessed Feb. 12, 2022).

[50] K. Kibaroglu, M. Sayginer, T. Phelps, and G. M. Rebeiz, 'A 64-Element 28-GHz Phased-Array Transceiver With 52-dBm EIRP and 8–12-Gb/s 5G Link at 300 Meters Without Any Calibration', *IEEE Trans. Microw.*

This article has been accepted for publication in IEEE Transactions on Antennas and Propagation. This is the author's version which has not been fully edited and content may change prior to final publication. Citation information: DOI 10.1109/TAP.2022.3178917

> REPLACE THIS LINE WITH YOUR PAPER IDENTIFICATION NUMBER (DOUBLE-CLICK HERE TO EDIT) <   14

Theory Tech., vol. 66, no. 12, pp. 5796–5811, Dec. 2018, doi: 10.1109/TMTT.2018.2854174.

[51] B. Rupakula, A. H. Aljuhani, and G. M. Rebeiz, 'ACPR Improvement in Large Phased Arrays With Complex Modulated Waveforms', *IEEE Trans. Microw. Theory Tech.*, vol. 68, no. 3, pp. 1045–1053, Mar. 2020, doi: 10.1109/TMTT.2019.2944824.

[52] N. Tervo *et al.*, 'Digital Predistortion of Phased-Array Transmitter With Shared Feedback and Far-Field Calibration', *IEEE Trans. Microw. Theory Tech.*, vol. 69, no. 1, pp. 1000–1015, Jan. 2021, doi: 10.1109/TMTT.2020.3038193.

[53] H. Wang, P. M. Asbeck, and C. Fager, 'Millimeter-Wave Power Amplifier Integrated Circuits for High Dynamic Range Signals', *IEEE J. Microw.*, vol. 1, no. 1, pp. 299–316, winter 2021, doi: 10.1109/JMW.2020.3035897.

[54] C. Fager, T. Eriksson, F. Barradas, K. Hausmair, T. Cunha, and J. C. Pedro, 'Linearity and Efficiency in 5G Transmitters: New Techniques for Analyzing Efficiency, Linearity, and Linearization in a 5G Active Antenna Transmitter Context', *IEEE Microw. Mag.*, vol. 20, no. 5, pp. 35–49, May 2019, doi: 10.1109/MMM.2019.2898020.

[55] S. Forestier, P. Bouysse, R. Quere, A. Mallet, J.-M. Nebus, and L. Lapierre, 'Joint Optimization of the Power-Added Efficiency and the Error-Vector Measurement of 20-GHz pHEMT Amplifier Through a New Dynamic Bias-Control Method', *IEEE Trans. Microw. Theory Tech.*, vol. 52, no. 4, pp. 1132–1141, Apr. 2004, doi: 10.1109/TMTT.2004.825745.